Journal of Materials Science: Materials in Electronics
https://doi.org/10.1007/s10854-020-03830-9

Ni-doped WO_3 flakes-based sensor for fast and selective detection of H_2S

Hong T. T. Nguyen[1,2] · Thi Hien Truong[3,4] · Tien Dai Nguyen[3,5] · Van Thai Dang[3] · Tuan V. Vu[1,2] · Son Tung Nguyen[6] · Xuan Phong Cu[7] · Thi Tu Oanh Nguyen[8]

Received: 5 March 2020 / Accepted: 18 June 2020

Abstract

In this work, we report on the synthesis of Ni-doped WO_3 flakes by the hydrothermal method. The physical and chemical properties of the synthesized Ni-doped WO_3 flakes were thoroughly investigated by scanning electron microscopy, transmission electron microscopy, energy-dispersive spectroscopy, Raman spectroscopy, photoluminescence spectrum, X-ray diffraction, X-ray photoelectron spectroscopy, and N_2 adsorption–desorption measurement, thereby confirming the effect of Ni doping on H_2S-sensing properties. The sensitivity to H_2S gas of Ni-doped WO_3 flakes showed short response/recovery times of 17 s/110 s, high stability, good selectivity, and low operating temperature of 250 °C. Due to the increasing surface defects and oxygen vacancies with the presence of Ni^{2+} ions in the structure of WO_3 flakes, the Ni-doped WO_3 sensor exhibited a better sensing of H_2S gas than the pristine WO_3 sensor. This result indicates that the Ni-doped WO_3 flake structure is promising for detecting H_2S gas as a selective, inexpensive, and outstanding sensor materials.

1 Introduction

The development of industry, transportation, and urbanization have increased the emission of toxic gases. Among them, hydrogen sulfide (H_2S) is known to have harmful effects on human health. In nature, H_2S is often produced from the decomposition of organic products in the absence of oxygen gas. United States Department of Labor indicated an 8-h limit for workers at a maximum concentration of 10 ppm H_2S. In addition to its high toxicity, H_2S is a highly explosive and flammable gas. Therefore, developing H_2S gas sensor is an essential requirement for the industry as well as for life. Many gas sensors with different principles and materials for the detection of H_2S gas have been developed [1–7]. Among them, metal oxide semiconductor (MOX)-based chemoresistive sensor exhibits superiority in chemical stability, durability, and response. From the aspect of gas-sensing materials, WO_3 is known to be an effective H_2S-sensing material for developing chemoresistive sensors [8–12]. However, like other metal oxides, the WO_3-based sensor remains inherent limitations that are high operating temperatures and poor selectivity. To enhance performances of the WO_3-based H_2S gas sensing, various methods were used. Mixing WO_3 with carbon material [13], hybrid structures [14], decorating with noble metals [15], modifying the morphology [16], and doping [17] issues are evaluated to be effective methods.

✉ Hong T. T. Nguyen
nguyenthithamhong@tdtu.edu.vn

✉ Tien Dai Nguyen
nguyentiendai@duytan.edu.vn

1 Division of Computational Physics, Institute for Computational Science, Ton Duc Thang University, Ho Chi Minh City, Vietnam

2 Faculty of Electrical & Electronics Engineering, Ton Duc Thang University, Ho Chi Minh City, Vietnam

3 Institute of Theoretical and Applied Research, Duy Tan University, Hanoi 100000, Vietnam

4 Graduate School, Duy Tan University, Da Nang 550000, Vietnam

5 Graduate University of Science and Technology, Vietnam Academy of Science and Technology, 18 Hoang Quoc Viet, Cau Giay, Hanoi, Vietnam

6 Faculty of Electrical Engineering Technology, Hanoi University of Industry, Hanoi 100000, Vietnam

7 Faculty of Vehicle and Energy Engineering, Le Quy Don Technical University, Hanoi 100000, Vietnam

8 Institute of Materials Science, Vietnam Academy of Science and Technology, 18 Hoang Quoc Viet, Cau Giay, Hanoi, Vietnam

Published online: 27 June 2020

However, some processes can be difficult to proceed in real production when sensors are manufactured in an industrial section. To date, using the hydrothermal method to modify the morphology in combination with in situ doping have been found to be a practical approach. The advantages of the hydrothermal method are simple equipment, high repeatability, and large-scale production ability. Cr-doped WO_3 microspheres have been synthesized in a one-step process using a simple hydrothermal method as an illustrative example [18]. Cr-doped WO_3 microspheres-based sensor showed a good response toward H_2S at the operating temperatures between 80 and 250 °C. This report indicated that using a one-step hydrothermal process can be an easy and efficient way to obtain outstanding H_2S gas-sensing properties, even at low temperatures. Moreover, the result revealed that high porous structure is sufficient to shorten the recovery time of the sensor, which was also reported by other authors [4, 19, 20]. Impressively, we investigated the gas-sensing performances of Ni-doped WO_3 flakes, which were also synthesized by the facial hydrothermal method. The Ni-doped WO_3 flakes-based sensor showed a stable, fast (17 s/110 s), and selective response toward H_2S at a low operating temperature of 250 °C. Besides that, a comparative study has also proceeded between the WO_3 fakes based sensor and Ni-doped WO_3 flakes-based sensor to find out the effect of Ni^{2+} ions on the H_2S-sensing properties of the latter. This result indicated that the outstanding H_2S-sensing properties of Ni-doped WO_3 flakes in comparison with WO_3 flakes, due to the increase of defects and oxygen vacancies on the surface of Ni-doped WO_3 flakes.

2 Experimental section

2.1 Synthesis of WO_3 and Ni-doped WO_3 flakes

WO_3 flak (S1 sample) was synthesized by the hydrothermal method. A fluorine-doped tin oxide glass (FTO/glass, Sigma Aldrich, TEC glass, 7 Ω/sq, 2 mm thick) substrate was used to grow WO_3 flakes on the surface. A mixing of 0.35 g of $Na_2WO_4{\cdot}2H_2O$ and 0.3 g of ammonium oxalate ($(NH_4)_2C_2O_4$) (from Sigma-Aldrich) were dissolved into both separated beakers with stirring. Then, two solutions were mixed, and an amount of 15 ml of hydrochloric acid with 3.0 M was dropped gradually into the mixture. FTO/glass substrate was cleaned and conducted to the autoclave with the precursor solution for hydrothermal synthesis at a temperature of 120 °C for 1 h. After cleaning, WO_3 flakes were collected by scraping WO_3 from the surface of the FTO, using a single edge blade.

Ni-doped WO_3 flakes (S2 sample) were also synthesized by the hydrothermal process, according to a reported procedure, elsewhere [21]. A mixing of 3.9 g of sodium tungstate dihydrate ($Na_2WO_4{\cdot}2H_2O$, ≥ 99%) and 2.85 g of Nickel(II) chloride hexahydrate ($NiCl_2{\cdot}6H_2O$), ≥ 97%) (from Sigma-Aldrich) were dissolved in 60 ml of DI water under vigorous stirring condition. Then the solution was poured into a Teflon-lined autoclave and heated at a temperature of 160 °C for 24 h. The resulting precipitate was cleaned and dried at a temperature of 70 °C overnight. To achieve the Ni-doped WO_3 flakes, the precipitate was immersed into 4.0 M HNO_3 for 24 h and stirred. After cleaning with DI water and absolute ethanol, the precipitate was dried and collected for the consequence procedures.

2.2 Material characterizations

The morphological and structural characterizations of WO_3 and Ni-doped WO_3 flakes (S1–S2 samples) were investigated by scanning electron microscope (SEM, Hitachi, S-4800) and X-ray diffraction (XRD, Bruker-D5005, Cu_Kα radiation ($\lambda = 0.1541$ nm). The compositions of samples were proved by energy-dispersive spectroscopy (EDS), which is integrated with SEM equipment. X-ray photoelectron spectroscopy (XPS, VG multi-lab 2000) was used for evaluating the contaminant level and the chemical states of elements of samples. X-ray source was used in XPS is a monochromatic Al Kα radiation (1486.7 eV). The XPS results were calibrated with the binding energy peak of adventitious carbon (284.8 eV). The deconvolution of O 1*s* peak was analyzed using the Thermo Avantage software, while baseline corrections were fitted using Shirley-type background correction. The optical properties of samples were investigated by the photoluminescence (PL) spectroscopy using an excitation wavelength of 300 nm with PL spectrophotometer (F-7000, Hitachi, Japan), and micro-Raman spectroscopy (ANDOR, SR-3030i) with an excitation wavelength of 532 nm and a power of 100 mW at room temperature. The surface areas of the samples were estimated by the Brunauer–Emmett–Teller (BET) method in which N_2 adsorption–desorption measurement was conducted using a 3Flex analyzer (ASAP 2420). Before measuring, the samples were outgassed at a temperature of 200 °C for 2 h.

2.3 Fabrication of sensors and gas-sensing measurement

For fabricating sensor, a suitable amount of S1 or S2 powder was mixed with absolute ethanol to form a paste. Al_2O_3 substrates with integrated Au electrodes were used to fabricate the sensors, using the bar-coating method. Then, the sensors were annealed in a furnace at a temperature of 500 °C for 2 h. The obtained sensors were labeled by S1 and S2-500 sensors, respectively. In order to optimize the annealing temperature, Ni-doped WO_3 sensor was furtherly annealed at 400 °C (S2-400 sensor) and 600 °C (S2-600 sensor). The S1

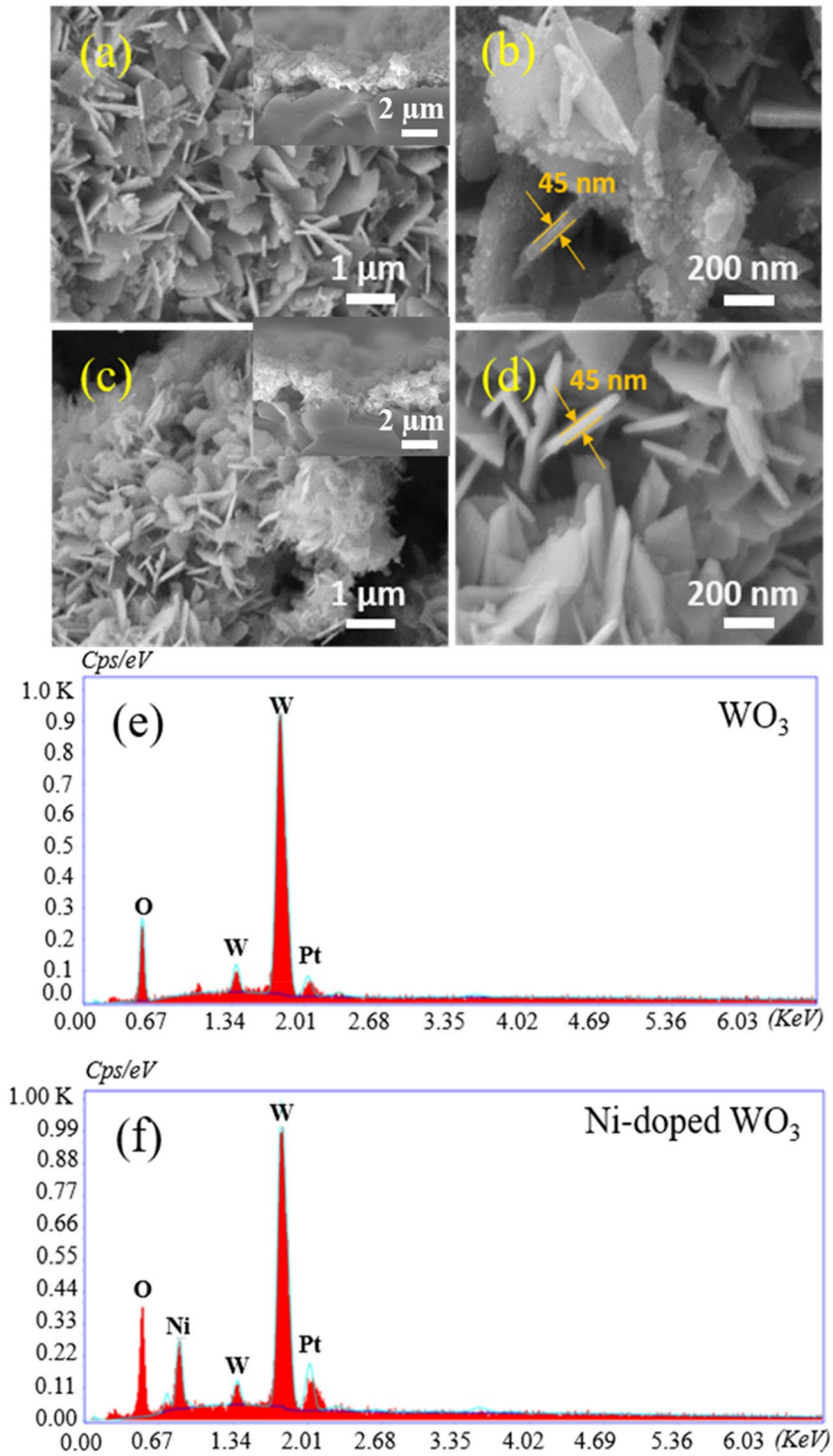

Fig. 1 **a** Low and high magnification SEM images of **a**, **b** WO_3 and **c**, **d** Ni-doped WO_3. The inserts show the cross-sectional views of respective sensors. Energy-dispersive spectra (EDS) of **e** WO_3 and **f** Ni-doped WO_3

and S2 powders were also annealed in the same condition for the related characterizations.

H_2S-sensing performances were investigated by recording real-time resistance of the sensors under the dry air and gas mixture of dry air and H_2S gas. The response of the sensor (S) is defined by $S = R_a/R_g$, where R_a and R_g are the resistance values of the sensor in the dry air and gas mixture, respectively. The temperature of the sensor was controlled by using an external heater, whereas the dry air and H_2S flow rates were controlled by mass flow controllers (MFC). The total flow rate in all the gas-sensing measurements was maintained at 300 sccm.

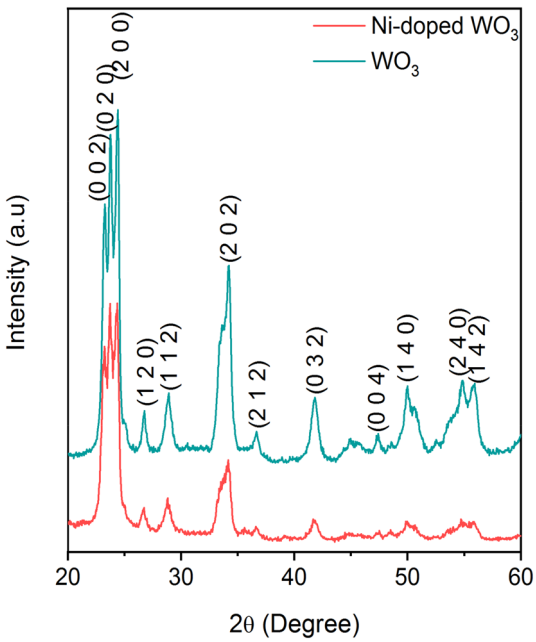

Fig. 2 X-ray diffraction spectra of WO_3 and Ni-doped WO_3

3 Results and discussion

3.1 Morphological, structural, and optical properties

Figure 1 shows the morphologies of S1 and S2 samples with the flake structure. The SEM images of the top view of both WO_3 flakes samples show the thicknesses with alike and roughly 45 nm, which are approximately two times the Debye length of WO_3 [22]. The samples are expected to get an outstanding gas-sensing response due to its optimum crystal size [22, 23] and high porosity. It is noted that the surface of the S2 sample is smoother than the S1 sample, whereas that of WO_3 was decorated with WO_3 nanoparticles. The inserts are the corresponding cross-sectional SEM images of samples which revealed the thicknesses of both samples are approximately 1 µm. Figure 1e, f presents the EDS results of S1 and S2 samples. The EDS spectrum confirms that the presence of the only W and O elements without other impurities in both samples. Besides that, the EDS observed a peak at approximate 0.85 keV of the S2 sample, which is ascribed to the emitting energy level of L_α of Ni atom, proved the appearance of Ni.

Figure 2 shows XRD patterns of S1 and S2 samples with similar diffraction peaks. The peaks at $2\theta = 23.12°$, 23.57°, 24.35°, 26.71°, 28.92°, 34.2°, 36.24°, 42.89°, 47.30°, 49.99°, 54.80°, and 55.89° are ascribed to the atomic planes of (0 0 2), (0 2 0), (2 0 0), (1 2 0), (1 1 2), (2 0 2), (2 1 2), (0 3 2), (0 0 4), (1 4 0), (2 4 0), and (1 4 2) of the monoclinic WO_3 structure (JCPDS 43-1035) [24]. The XRD patterns of S1–S2 samples also indicate no peaks of the new phase that can be detected within the resolution ability of the diffraction equipment. As a result, we can conclude that the Ni ions have doped into the crystal lattice of WO_3 without formatting a new phase on it. Besides that, the ionic radius of W^{6+} (0.06 nm) and Ni^{2+} (0.069 nm) are a favorable condition for the doping process can be taken place [25]. The substitution of W^{6+} ion by Ni^{2+} ion led to a delight disturbance in the crystalline structure of WO_3, which resulted in an intensity decrease of the peaks in the large diffraction angle region (from 50 to 60°) in the XRD pattern of S2 sample.

Figure 3a shows XPS spectra of S1 and S2 samples, which confirmed the contaminant level in these samples. A small peak of Ni element was detected in the survey spectrum of the S2 sample. The high-resolution XPS spectrum of Ni revealed more clearly that Ni element exists at Ni^{2+} state with characteristic peaks of Ni $2p_{3/2}$ and Ni $2p_{1/2}$ at 856.45 eV and 873.97 eV, respectively, as shown in Fig. 3b [26]. The peaks of W $4f_{7/2}$ (at 35.72 eV) and W $4f_{5/2}$ (at 37.9 eV) can be ascribed to the existence of W^{6+} chemical state in WO_3 [26], as shown in Fig. 3c. Due to the presence of Ni^{2+} in the WO_3 crystalline structure, the peaks of the S2 sample were shifted peaks toward lower binding energy [18, 25]. The effect of electronegativity due to the presence of Ni^{2+} is considered as a reason for the binding energy shift of W 4*f* [27]. Therefore, this result is good evidence, which proved the doping of Ni into the crystal lattice of WO_3. The doping of Ni^{2+} in WO_3 also led to the density change of oxygen vacancies, as well as the distribution of oxygen ions on the surface of WO_3 [25], which has a strong effect on gas-sensing properties. In Fig. 3d, the O 1*s* peak was deconvoluted into oxygen in stoichiometric WO_3 (peak *N*° of 1 at 530.9 eV), oxygen in non-stoichiometric WO_{3-x} (peak *N*° of 2 at 531.8 eV) and oxygen in the surface hydroxyl group (peak *N*° of 3 at 532.8 eV) [28–31]. The O 1*s* peak at 531.8 eV can be used as an indirect estimation to evaluate the oxygen vacancy level on the surface of the S2 sample [29]. The S2 sample showed a significant increase in peak *N*° of 2, which indicated that the S2 sample contains a larger amount of oxygen vacancies in comparison with that of WO_3. The amount of Ni in the S2 sample was 2.52 at.% calculated from the area ratio of characteristic peaks of the elements, using Thermo Avantage software. The calculating process was calibrated with relative sensitivity factor (RSF) of each element.

Figure 4a shows the photoluminescence (PL) spectrum of S1–S2 samples at room temperature. There was a peak at 450 nm (2.75 eV) of both samples, which be attributed to the recombination of free excitons and ascribed to near band edge (NBE) emission [32]. There was no shift of the NBE peaks that would be observed between two samples, thereby no significant difference in the bandgap. According to our acknowledgment, the bandgap of semiconductor

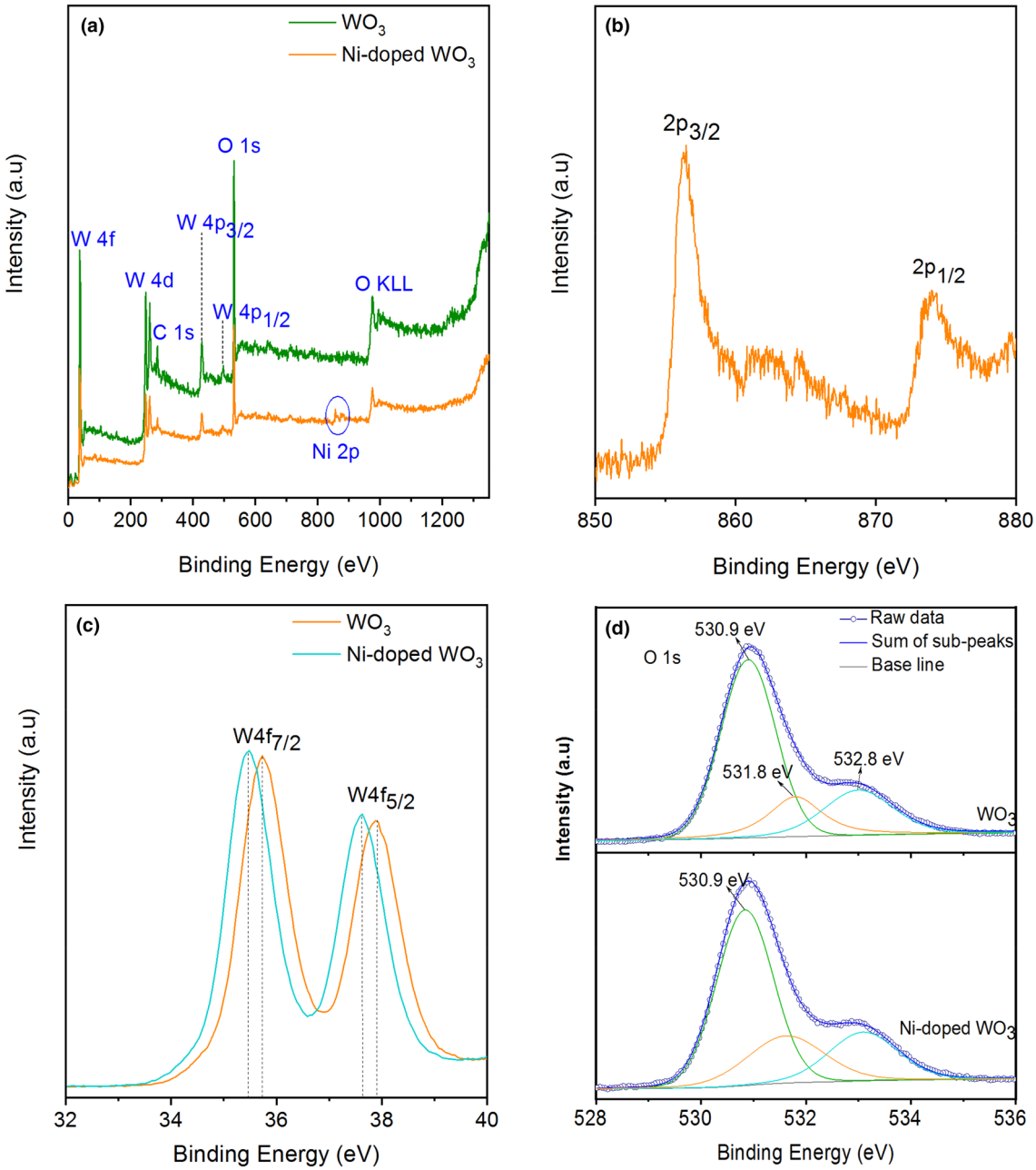

Fig. 3 **a** X-ray photoelectron spectroscopy (XPS) spectra of WO_3 and Ni-doped WO_3. **b**, **c** High-resolution spectra of Ni 2*p* and W 4*f*. **d** O 1*s*—level XPS deconvolution spectra of WO_3 and Ni-doped WO_3

materials strongly depends on the size when the dimension of materials down to nano-size [33]. This result confirmed that the similar dimension of S1–S2 samples again (Fig. 1). The lower PL intensity of Ni-doped WO_3 (S2 sample) is attributed to the lower recombination rate of the photo-generated electrons and holes, which is strongly affected by the higher defect density [34]. This result is consistent with the results received from XPS. The surface defects and oxygen vacancies are essential factors that significantly impact on the surface reaction between H_2S and pre-adsorbed oxygen ions, as well as the direct absorption of H_2S on the WO_3 surface. As a result, the change of these factors will create a significant change in the response of the sensor [35]. The effect of surface defects and oxygen vacancies of Ni-doped WO_3 on the Raman spectrum was also investigated, as shown in Fig. 4b. The Raman spectrum of WO_3 includes four modes at 256.2, 319.8, 708.7, and 802.5 cm^{-1} corresponding to the Raman active of the monoclinic WO_3 structure. Two higher Raman peak positions at 708.7 and 802.5 cm^{-1} are attributed to the W–O–W stretching frequencies, while two

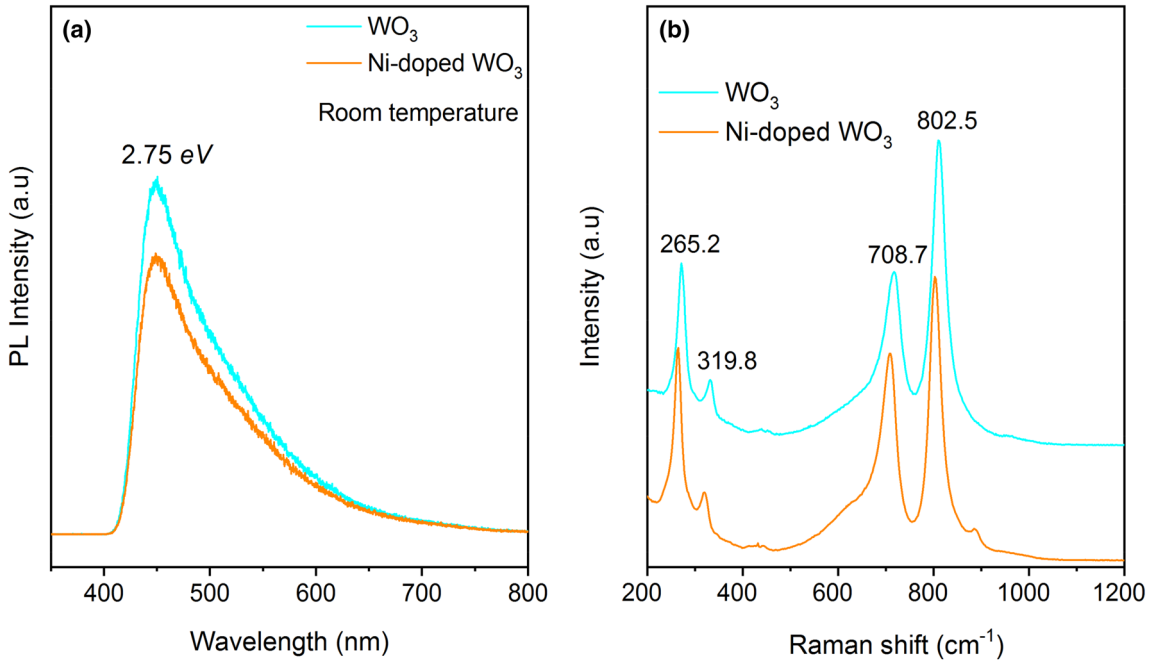

Fig. 4 **a** Photoluminescence spectrum and **b** Raman spectra of WO_3 and Ni-doped WO_3 at room temperature

weaker peaks at 256.2, 319.8 cm^{-1} are assigned to bending vibration modes in WO_3 [36, 37]. There is a significant shift in Raman spectrum of S2 sample comparing to that of WO_3 due to the surface defects, oxygen vacancies, and the rearrangement of oxygen ions on the surface of S2 samples to obtain charge neutrality [38–41]. Due to the increase of the surface defects and oxygen vacancies, which have a strong effect on the number of active sites for H_2S adsorption, the number of pre-absorbed oxygen ions, as well as its distribution on the surface of WO_3. These changes play an important role in the enhancement of the number of H_2S molecules that can be absorbed, thereby improving the detection of H_2S gas of S2 sample as shown later. Furthermore, it should be noted that the dimension of flakes in S1 and S2 samples are similar, whereas the S2 sample are further decorated by WO_3 nanoparticles with diameters of 10–20 nm, as shown in Fig. 1a–d. Therefore, the improved Raman intensity of S2 sample should be considered under the surface reactions instead of the difference in the surface area between S1 and S2 samples.

3.2 Gas-sensing characteristics and sensing mechanism

The gas-sensing properties of Ni-doped WO_3 sensor (S2 sample) are firstly investigated with various operating temperatures from 150 to 350 °C. In Fig. 5a, b, H_2S-sensing results indicated that the response and recovery speed of the S2-500 sample are faster than those of the S1 sample at an operating temperature below 250 °C. However, there is almost no difference between them when the operating temperature rises. Generally, the fast response/recovery of S1 and S2-500 sensors was contributed to the high porosity of the flake structure that caused the quick diffusion of H_2S and O_2. It is noted that the S2-500 sensor shows outstanding responses in comparison with the S1 sensor at all operating temperatures, as shown in Fig. 5c. This result can be understood due to surface defects and oxygen vacancies, as discussed in the previous section. The presence of Ni^{2+} in the crystal structure of WO_3 caused the change of defect and oxygen vacancy density and distribution, thereby leading to the change of activated energy to adsorption and desorption processes of H_2S molecules on the surface of S2 sample.

Therefore, when the operating temperature is low, thermal energy is more useful for the S2 sample, which was proved by the faster response-recovery process and the higher response of the S2 sample at the temperature below 250 °C. At the higher operating temperatures, thermal energy exceeds the necessary limit required for effective adsorption–desorption process for both sensors. Therefore, response–recovery speeds of sensors were observed to be no different in the high-temperature region. Figure 5d compares the responses between WO_3 and Ni-doped WO_3 sensors operated at 250 °C toward 10 ppm H_2S, which indicate the outstanding sensing-behavior of the latter. Figure 6 shows the results of N_2 adsorption–desorption measurement, which evaluated the effect of surface area on gas-sensing properties. The insignificant difference between the

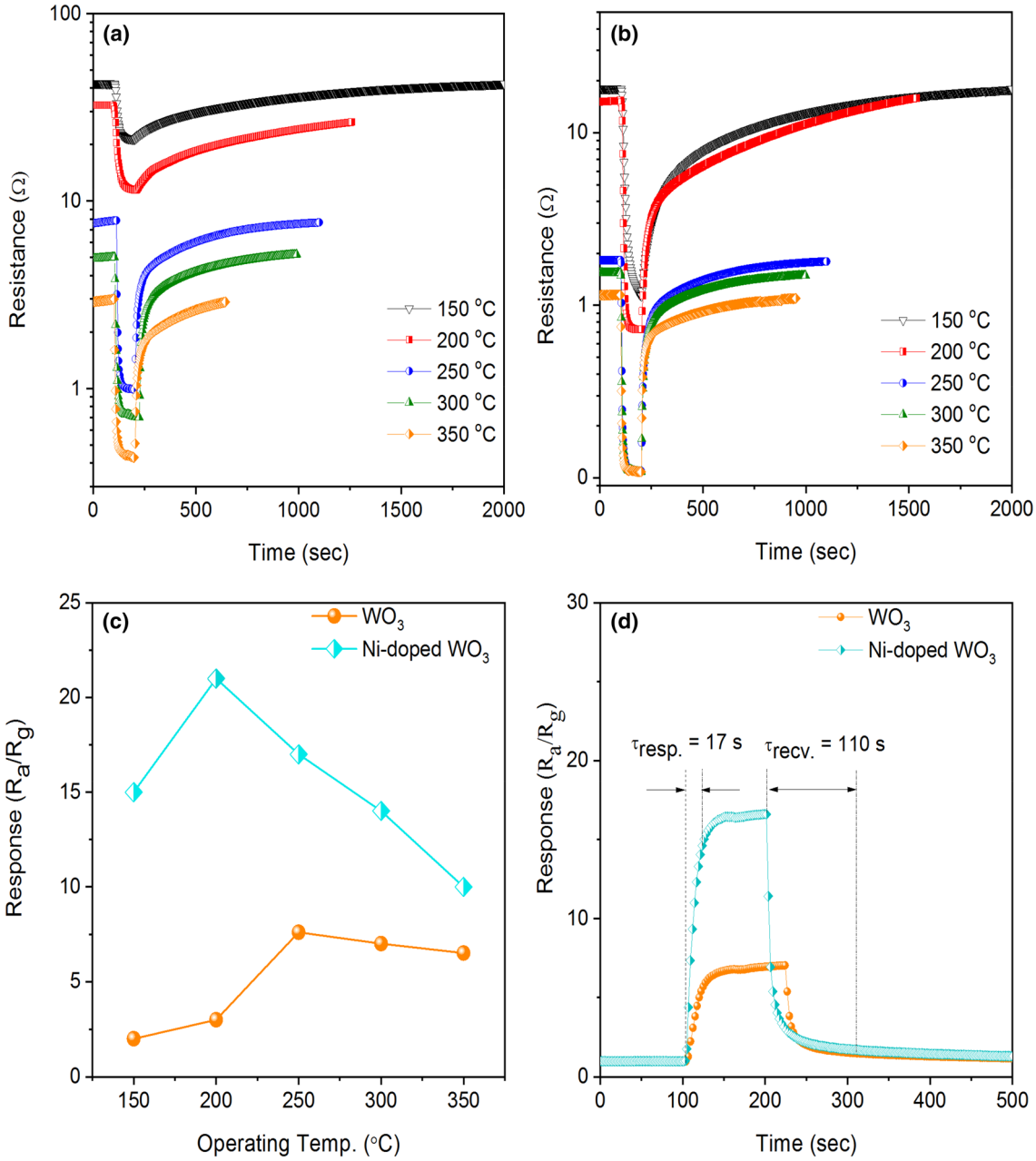

Fig. 5 **a** Transient resistance vs time curves of **a** WO_3 and **b** Ni-doped WO_3 sensors toward 10 ppm H_2S measured at the different operating temperatures from 150 to 350 °C, **c** the comparison of responses between WO_3 and Ni-doped WO_3 sensors at different operating temperatures, **d** the response and recovery times of Ni-doped WO_3 sensor estimated from the dynamic response curves at the operating temperature of 250 °C

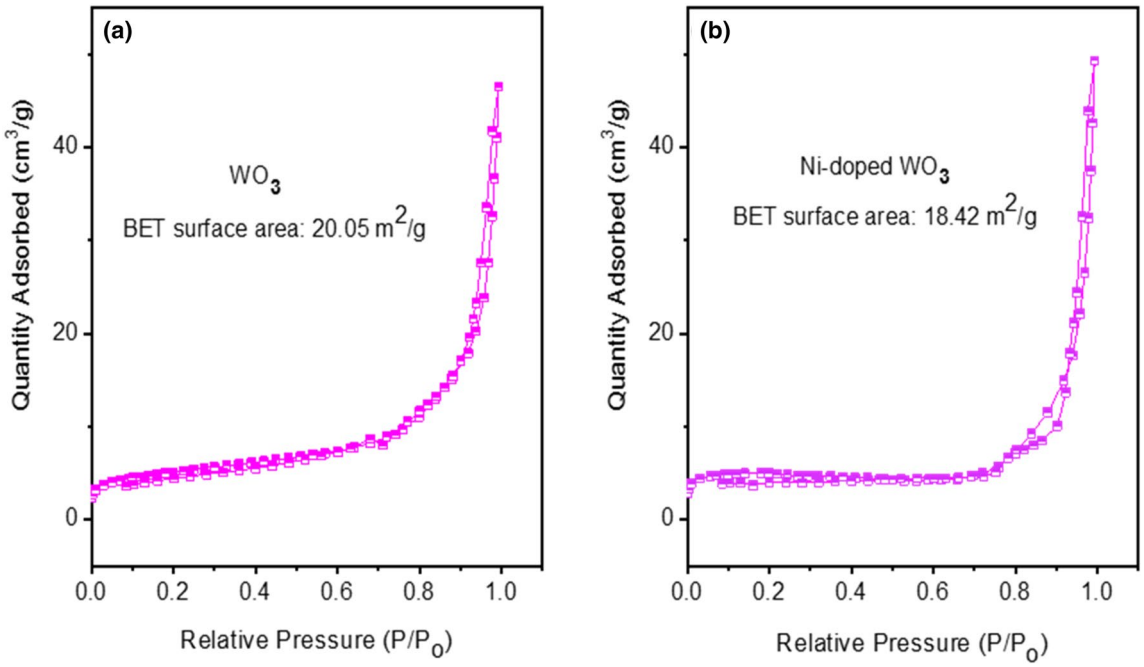

Fig. 6 N_2 adsorption–desorption curves of **a** WO_3 and **b** Ni–WO_3

BET surface areas revealed that the surface area was not a key factor leading to different responses between two sensors. These results further confirm the effect of Ni doping on the outstanding sensing performance of the Ni-doped WO_3 sensor.

In this study, we also optimized the annealing temperature for detecting H_2S gas, and the results are shown in Fig. 7. The result indicated that the S2-500 sample shows a higher response than others. When annealing temperature is raised, the crystallinity of the WO_3 flake becomes better, which will enhance the charge mobility. Dislocation and point defects in WO_3 were decreased through the diffusion process at high temperature [42–45], thereby reducing the lattice strain. As a consequence, electron mobility is enhanced, which reported by several authors [46, 47]. Because of that, the electron-support rate to the surface of WO_3 for NO_2 adsorption (response process) and O_2 adsorption (recovery process) become faster. Therefore, the response of the sensor will increase, whereas response-recovery time will decrease. However, when the annealing temperature is too high, the surface defects and area are reduced significantly. As a result, the response of the S2-600 sensor will decrease with the decrease in the number of active sites for H_2S absorption. In Fig. 7d, the H_2S-sensing results revealed that S2-500 reached the highest responses at all examined concentrations of H_2S in comparison with others [9, 12, 13, 48–52]. Notably, the response of the S2-500 sensor toward 10 ppm H_2S was 17 times, while those are 13 and 11 for S2-400 and S2-600, respectively. Therefore, the S2-500 sensor was chosen for further investigations. In order to highlight the result of this study, the H_2S-sensing properties of WO_3-based gas sensors from the literature are summarized in Table 1. Obviously, Ni-doped WO_3 flakes-based sensor showed a significant response with a fast response-recovery time at a lower operating temperature. The fact that the stability and selectivity of the sensor are important factors. Therefore, we also investigated those characterizations of the S2-500 sensor, as shown in Fig. 8. The sensor showed good short-time stability and selectivity. It should be noted that the response of comparative gases is neglectful. However, the concentrations of H_2, CH_4, and CO gases are 25 times larger than that of H_2S gas. A small response was detected to 10 ppm of NH_3 gas. However, the response is minimal in comparison with the response of H_2S gas. The sensing performance of S2-500 after 6 months was measured to evaluate the long-term stability of the sensor. Figure 9a displays the response curves of the S2-500 sensor and S2-500 after 6 months, whereas the corresponding responses are shown in Fig. 9b. Clearly, the response/recovery times are alike, but the response of the sensor was slightly decreased after 6 months. Besides, a slight shift of base resistance was observed, which could be due to the contact. The reason for the reduction in the response is unknown and needs further investigations. It is worth that the response of the S2-500 sensor still shows

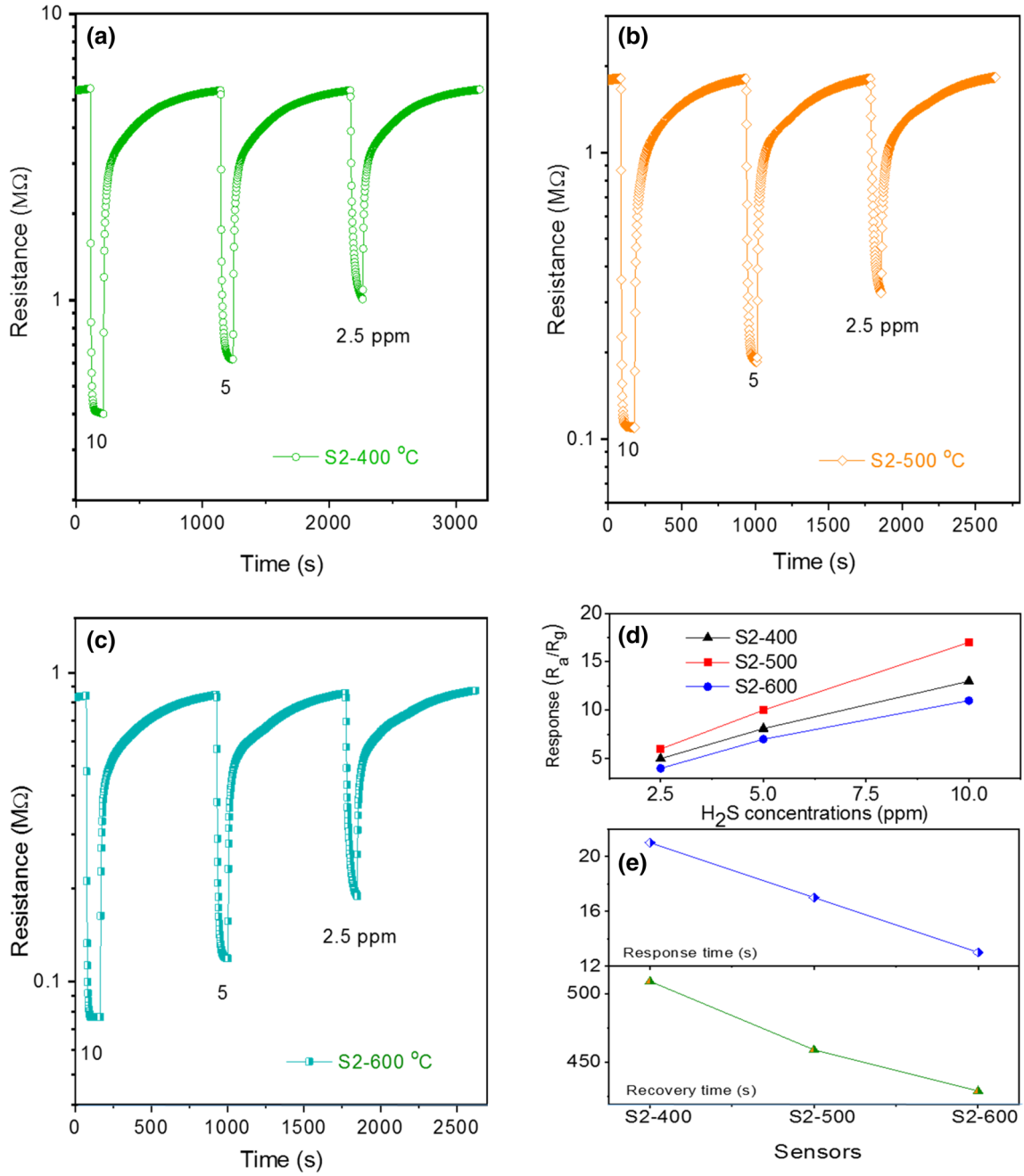

Fig. 7 **a–c** H_2S-sensing transient of the Ni-doped WO_3 flake sensor annealed at different annealing temperatures from 400 to 600 °C measured at an operating temperature of 250 °C, **d** Summaries of the response of the sensors toward various H_2S concentrations. **e** Typical response-recovery time of the sensors measured at 250 °C and 10 ppm H_2S

excellent linearity. Therefore, it will be an advantage for the calibration of a real device. Furthermore, the sensor also exhibited excellent short-term repeatability after 6 months (Fig. 9c). The reproducibility was also investigated with three sensors, as shown in Fig. 10a. Those sensors indicated that the transient response curves are similar to an insignificant distribution of the base resistance, as shown in Fig. 10b. The responses between the three sensors also exhibited a small distribution. A small difference in response and baseline between these sensors

Table 1 H_2S-sensing properties of WO_3-based gas sensors

Materials	[H_2S]/ppm	T (°C)	Response	t_{res}/t_{rec}	References
WO_3 nanowires	100	300	1.84	–/–	[48]
CuO–WO_3 nanowires	100	300	6.72	–/–	[48]
3D rGO/h-WO_3	1	330	10.8	–/–	[13]
Cu_2O–WO_3 nanoneedles	5	390	27.5	2 s/684 s	[49]
CuO–WO_3 thin film	10	300	534	5 s/24 min	[50]
CuO/WO_3 composite	5	100	223	70 s/450 s	[12]
WO_3 nanowires	10	400	104	–/–	[51]
WO_3 nanorods	10	350	20	2.6 min/18.5 min	[9]
Ru/WO_3 nanorods	10	350	192	0.8 s/11 min	[9]
WO_3 nanoparticles	1	250	3.5	–/–	[52]
Ni-doped WO_3 flakes	10	250	17	17 s/110 s	This study

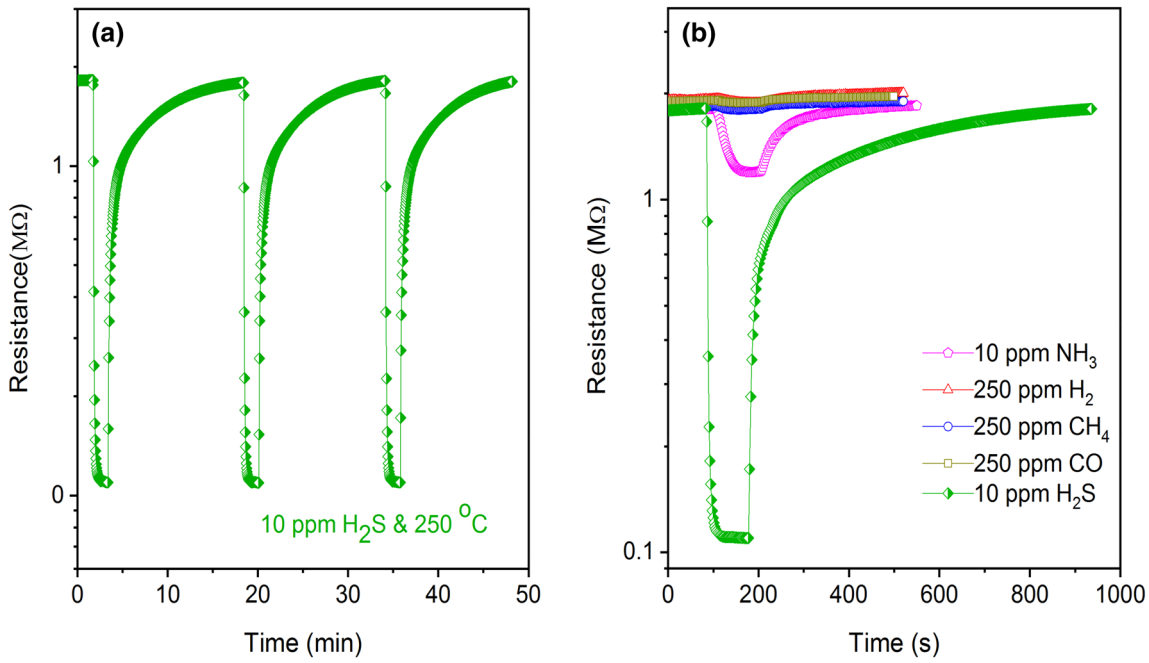

Fig. 8 **a** Short-time stability and **b** the selectivity of S2-500 sensor underexposing H_2S gas

is derived from limitations in precisely controlling a thickness of the sensors. However, this limitation can be resolved with the industrial processes, which are always controlled strictly.

4 Conclusion

In conclusion, Ni-doped WO_3 flakes have synthesized by the hydrothermal method for detecting H_2S gas with stable, fast, and selective. The Ni-doped WO_3 sensor showed an outstanding gas-sensing property in comparison with the pristine WO_3 sensor, which is supported by the increase of surface defects and oxygen vacancies due to the presence of Ni^{2+} ions in the WO_3 structure. High stability, simple, repeatable fabrication method, and short response/recovery times (17 s/110 s) of the Ni-doped WO_3 sensor are remarkable properties at a low operating temperature of 250 °C. However, the effect of environmental humidity on the performance of the sensor needs to be further investigated for the development of a real H_2S sensor.

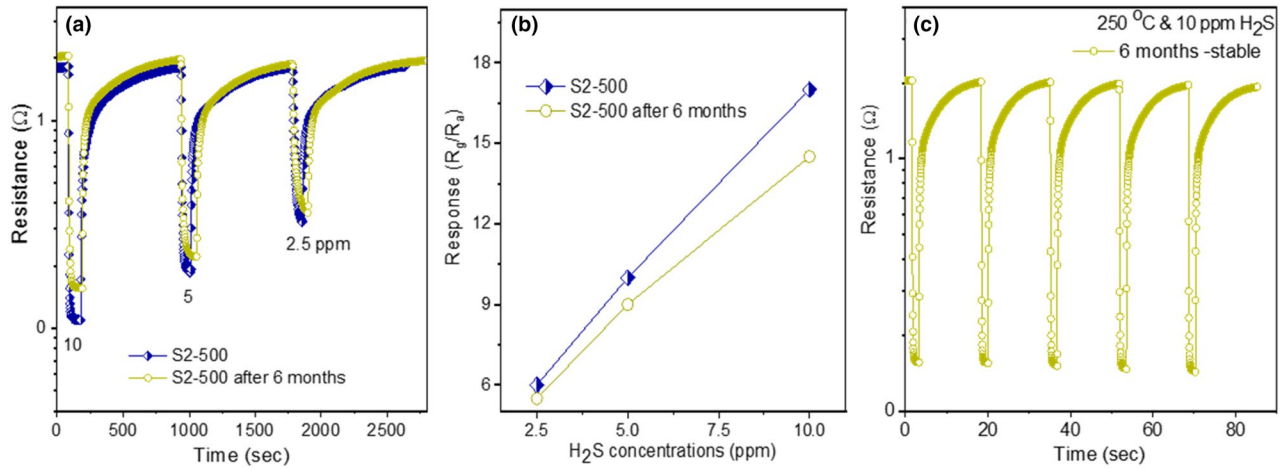

Fig. 9 **a** Response vs. time curves of S2-500 sensor toward H_2S measured as soon as fabricating and after storing 6 months. **b** Summaries of the response of the sensor derived from **a**. **c** The stability of the sensor S2-500 after 6 months

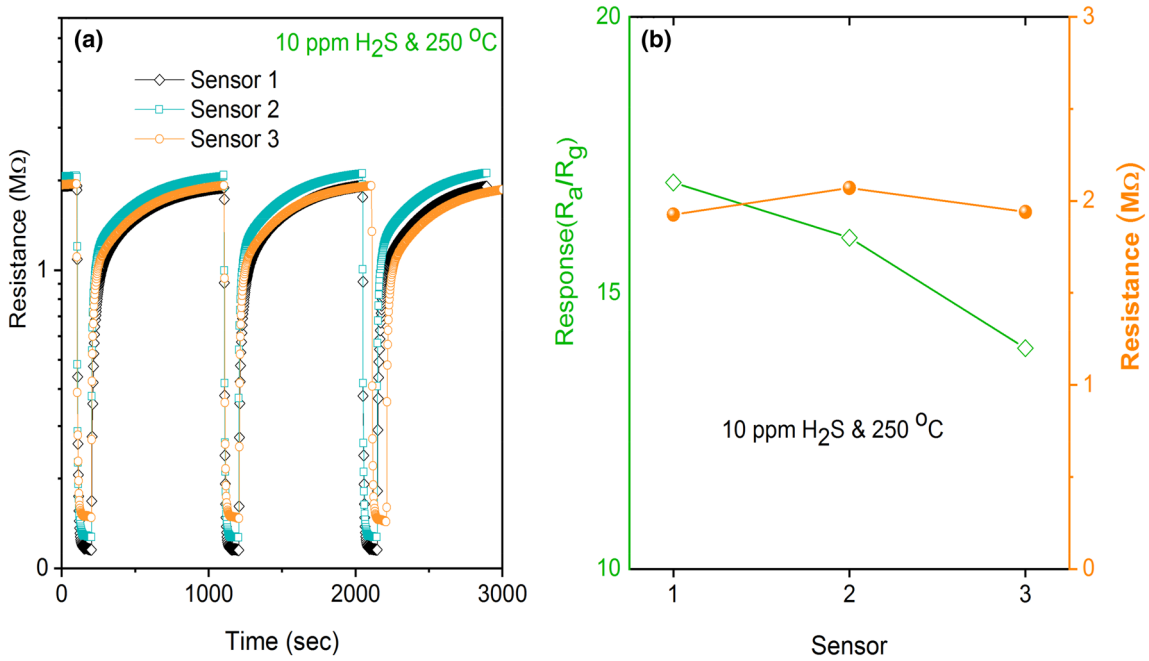

Fig. 10 **a** Reproducibility of the S2-500 sensor was examined with three different sensors. **b** Summaries of the responses and base resistances of three S2-500 sensors

Acknowledgements This work was funded by Graduate University of Science and Technology, Vietnam Academy of Science and Technology under Grant Number GUST.STS.ĐT2020-HH10.

Compliance with ethical standards

Conflict of interest The authors declare no competing financial interests.

References

1. P.S. Kolhe et al., Gas sensing performance of Al doped ZnO thin film for H2S detection. J. Alloy. Compd. **748**, 6–11 (2018)
2. W. Luo et al., A surface acoustic wave H2S gas sensor employing nanocrystalline SnO_2 thin film. Sens. Actuators B **176**, 746–752 (2013)
3. R. Tabassum, S.K. Mishra, B.D. Gupta, Surface plasmon resonance-based fiber optic hydrogen sulphide gas sensor utilizing

Cu–ZnO thin films. Phys. Chem. Chem. Phys. **15**(28), 11868–11874 (2013)
4. J. Tan et al., ZIF-67 MOF-derived unique double-shelled Co_3O_4/$NiCo_2O_4$ nanocages for superior Gas-sensing performances. Sens. Actuators B **303**, 127251 (2020)
5. C. Wu et al., A novel hydrogen sulfide gas sensor apply in tunnel construction. Sci. Adv. Mater. **11**(1), 112–115 (2019)
6. Z. Zeng et al., The detection of H_2S at room temperature by using individual indium oxide nanowire transistors. Nanotechnology **20**(4), 045503 (2008)
7. S. Hussain et al., Novel gravel-like $NiMoO_4$ nanoparticles on carbon cloth for outstanding supercapacitor applications. Ceram. Int. **46**(5), 6406–6412 (2020)
8. M.-H. Kim et al., Bimodally porous WO_3 microbelts functionalized with Pt catalysts for selective H_2S sensors. ACS Appl. Mater. Interfaces **10**(24), 20643–20651 (2018)
9. V. Kruefu et al., Ultra-sensitive H_2S sensors based on hydrothermal/impregnation-made Ru-functionalized WO_3 nanorods. Sens. Actuators B **215**, 630–636 (2015)
10. S. Poongodi et al., Electrodeposition of WO_3 nanostructured thin films for electrochromic and H_2S gas sensor applications. J. Alloy. Compd. **719**, 71–81 (2017)
11. M. Takács et al., WO_3 nano-rods sensitized with noble metal nano-particles for H_2S sensing in the ppb range. Mater. Res. Bull. **84**, 480–485 (2016)
12. L. Yin et al., Construction and enhanced low-temperature H_2S-sensing performance of novel hierarchical CuO@WO_3 nanocomposites. J. Alloy. Compd. **785**, 367–373 (2019)
13. J. Shi et al., Facile synthesis of reduced graphene oxide/hexagonal WO_3 nanosheets composites with enhanced H_2S sensing properties. Sens. Actuators B **230**, 736–745 (2016)
14. W. Yu et al., CuO/WO_3 hybrid nanocubes for high-responsivity and fast-recovery H_2S sensors operated at low temperature. Part. Part. Syst. Charact. **33**(1), 15–20 (2016)
15. Q. Xiang et al., Au nanoparticle modified WO_3 nanorods with their enhanced properties for photocatalysis and gas sensing. J. Phys. Chem. C **114**(5), 2049–2055 (2010)
16. M. He et al., Highly sensitive and selective H_2S gas sensors based on flower-like WO_3/CuO composites operating at low/room temperature. J. Alloy. Compd. **788**, 36–43 (2019)
17. T. Vilic, E. Llobet, Nickel doped WO_3 nanoneedles deposited by a single step AACVD for gas sensing applications. Proc. Eng. **168**, 206–210 (2016)
18. Y. Wang et al., Low-temperature H_2S detection with hierarchical Cr-doped WO_3 microspheres. ACS Appl. Mater. Interfaces **8**(15), 9674–9683 (2016)
19. N. Van Hoang et al., Facile on-chip electrospinning of ZnFe2O4 nanofiber sensors with excellent sensing performance to H2S down ppb level. J. Hazard. Mater. **360**, 6–16 (2018)
20. Y. Zhao et al., Porous CuO/SnO_2 composite nanofibers fabricated by electrospinning and their H2S sensing properties. Sens. Actuators B **165**(1), 82–87 (2012)
21. S. Li et al., The room temperature gas sensor based on Polyaniline@flower-like WO_3 nanocomposites and flexible PET substrate for NH_3 detection. Sens. Actuators B **259**, 505–513 (2018)
22. J. Kukkola et al., Room temperature hydrogen sensors based on metal decorated WO_3 nanowires. Sens. Actuators B **186**, 90–95 (2013)
23. J. Shieh et al., WO3 and WTiO thin-film gas sensors prepared by sol–gel dip-coating. Sens. Actuators B **86**(1), 75–80 (2002)
24. J. Guo et al., Synthesis of WO_3@Graphene composite for enhanced photocatalytic oxygen evolution from water. RSC Adv. **2**(4), 1356–1363 (2012)
25. A.A. Dakhel, H. Ashoor, Synthesis of semiferromagnetic Ni-doped WO3 nanoparticles by precipitation method: evaluation of effect of treatment in hydrogen gas. Mater. Chem. Phys. **230**, 172–177 (2019)
26. J.F. Moulder, Physical electronics, in *Handbook of X-ray photoelectron spectroscopy*, ed. by J. Chastain, J. Roger, C. King (Physical Electronics, Inc., Chanhassen, 1995)
27. A.P. Grosvenor et al., New interpretations of XPS spectra of nickel metal and oxides. Surf. Sci. **600**(9), 1771–1779 (2006)
28. S. Bai et al., Gas sensing properties of Cd-doped ZnO nanofibers synthesized by the electrospinning method. J. Mater. Chem. A **2**(39), 16697–16706 (2014)
29. Y.-A. Lee et al., Highly sensitive gasochromic H_2 sensing by nano-columnar WO_3–Pd films with surface moisture. Sens. Actuators B **238**, 111–119 (2017)
30. M. Tong et al., Facile preparation of amorphous carbon-coated tungsten trioxide containing oxygen vacancies as photocatalysts for dye degradation. J. Mater. Sci. **54**(15), 10656–10669 (2019)
31. T.K.H. Ta et al., Surface functionalization of WO_3 thin films with (3-Aminopropyl)triethoxysilane and succinic anhydride. J. Electron. Mater. **46**(6), 3345–3352 (2017)
32. H. Zhang et al., Template-free facile preparation of monoclinic WO_3 nanoplates and their high photocatalytic activities. Appl. Surf. Sci. **305**, 274–280 (2014)
33. R. Marotti et al., Crystallite size dependence of band gap energy for electrodeposited ZnO grown at different temperatures. Sol. Energy Mater. Sol. Cells **90**(15), 2356–2361 (2006)
34. F. Mehmood et al., Structural, Raman and photoluminescence properties of Fe doped WO_3 nanoplates with anti cancer and visible light driven photocatalytic activities. J. Alloy. Compd. **728**, 1329–1337 (2017)
35. Z. Lin et al., The effect of Ni doping concentration on the gas sensing properties of Ni doped SnO2. Sens. Actuators B **239**, 501–510 (2017)
36. L. Xu, M.-L. Yin, S.F. Liu, Agx@WO_3 core–shell nanostructure for LSP enhanced chemical sensors. Sci. Rep. **4**, 6745 (2014)
37. C. Santato et al., Crystallographically oriented mesoporous WO_3 films: synthesis, characterization, and applications. J. Am. Chem. Soc. **123**(43), 10639–10649 (2001)
38. J. Dhanalakshmi et al., Investigation of oxygen vacancies in Ce coupled TiO_2 nanocomposites by Raman and PL spectra. Adv. Nat. Sci. **8**(1), 015015 (2017)
39. J. Li, J. Zhu, X. Liu, Synthesis, characterization and enhanced gas sensing performance of WO_3 nanotube bundles. New J. Chem. **37**(12), 4241–4249 (2013)
40. F. Mehmood et al., Ni doped WO_3 nanoplates: an excellent photocatalyst and novel nanomaterial for enhanced anticancer activities. J. Alloy. Compd. **746**, 729–738 (2018)
41. H. He et al., MoS_2/TiO_2 edge-on heterostructure for efficient photocatalytic hydrogen evolution. Adv. Energy Mater. **6**(14), 1600464 (2016)
42. M. Lamers et al., Formation and suppression of defects during heat treatment of $BiVO_4$ photoanodes for solar water splitting. J. Mater. Chem. A **6**(38), 18694–18700 (2018)
43. S. Nakakura et al., Cationic defect engineering for controlling the infrared absorption of hexagonal cesium tungsten bronze nanoparticles. Inorg. Chem. **58**(14), 9101–9107 (2019)
44. G. Parsons et al., Reduction of defects by high temperature annealing (150 °C–240 °C) in hydrogenated amorphous silicon films deposited at room temperature. J. Non-Cryst. Solids **114**, 178–180 (1989)
45. Z. Tanasta et al., *Reduction of Defects on Microstructure Aluminium Nitride Using High Temperature Annealing Heat Treatment in IOP Conference Series: Materials Science and Engineering* (IOP Publishing, Bristol, 2018)
46. V.W. Chin, T. Tansley, Alloy scattering and lattice strain effects on the electron mobility in $In_{1-x}Ga_xAs$. Solid-State Electr. **34**(10), 1055–1063 (1991)

47. M. Finetti, R. Galloni, A. Mazzone, Influence of impurities and crystalline defects on electron mobility in heavily doped silicon. J. Appl. Phys. **50**(3), 1381–1385 (1979)
48. S. Park et al., H_2S gas sensing properties of CuO-functionalized WO_3 nanowires. Ceram. Int. **40**(7), 11051–11056 (2014)
49. F.E. Annanouch et al., Aerosol-assisted CVD-grown WO_3 nanoneedles decorated with copper oxide nanoparticles for the selective and humidity-resilient detection of H_2S. ACS Appl. Mater. Interfaces **7**(12), 6842–6851 (2015)
50. N.S. Ramgir et al., Selective H_2S sensing characteristics of CuO modified WO_3 thin films. Sens. Actuator B **188**, 525–532 (2013)
51. N. Kaur et al., Integration of VLS-grown WO_3 nanowires into sensing devices for the detection of H_2S and O_3. ACS Omega **4**(15), 16336–16343 (2019)
52. R. Ionescu et al., Low-level detection of ethanol and H_2S with temperature-modulated WO_3 nanoparticle gas sensors. Sens. Actuators B **104**(1), 132–139 (2005)